Quantitative analysis of seismic wave propagation anomalies in azimuth and apparent slowness at Deception Island volcano (Antarctica) using seismic arrays

A. García Yeguas,[1,2] J. Almendros,[1,2] R. Abella[3] and J. M. Ibáñez[1,2]

[1]*Departamento de Física Teórica y del Cosmos, Universidad de Granada, Spain. E-mail: alm@iag.ugr.es*
[2]*Instituto Andaluz de Geofísica, Universidad de Granada, Spain*
[3]*Instituto Geográfico Nacional, Madrid, Spain*

SUMMARY

We analyse shot data recorded by eight seismic arrays during an active-source seismic experiment carried out at Deception Island (Antarctica) in 2005 January. For each source we estimate the apparent slowness and propagation azimuth of the first wave arrival. Since both source and receiver positions are accurately known, we are able to interpret the results in terms of the effect of the heterogeneities of the medium on wave propagation. The results show the presence of significant propagation anomalies. Nearby shots produce large apparent slowness values above 0.6 s km^{-1}, while distant shots produce small values, down to about 0.15–0.20 s km^{-1}. These values are different for each array, which shows the importance of the local structure under the receiver. The spatial distributions of apparent slowness are not radial as we would expect in a flat-layered medium. And again, these distributions are different for each array. The azimuth anomalies defined as the difference between the empirical estimates and the values expected in a 1-D model (i.e. the source-array directions) suggest ubiquitous wave front distortions. We have detected both positive and negative anomalies. For some shot-array geometries, azimuth anomalies are quite large with values up to 60°. The distribution of the anomalies depends on the position of the array. Some of these features can be interpreted in terms of a shallow magma chamber and shallow rigid bodies imaged by high-resolution seismic tomography. However several details remain unexplained. Further work is required, including modelling of synthetic wavefields on realistic models of Deception Island and/or apparent slowness vector tomography.

Key words: Controlled source seismology; Body waves; Volcano seismology; Wave propagation; Antarctica.

1 INTRODUCTION

Volcanic environments are highly heterogeneous media at different length scales. From a seismic point of view, they are characterized by materials with a variety of seismic wave velocities and strong impedance contrasts among different parts of the medium. These heterogeneities may significantly affect seismic wave propagation, producing strong path effects such as the occurrence of intense attenuation, refractions, reflections and scattering processes. The presence of a sharp topography may further affect the seismic wavefield in a way that it is difficult to assess *a priori*.

The intricacies and distortions of seismic wavefields produced by volcanic structures can be detected using different seismological techniques. For example, we can detect delays in the arrival times of *P* and *S* waves that are related to the heterogeneity of the velocity structure. The measurement of these delays at a distributed network of seismic stations constitutes the basis of the traveltime tomography method, widely applied in volcanic areas (e.g. Benz *et al*. 1996; Dawson *et al*. 1999; Patane *et al*. 2002; Monteiller *et al*. 2005; Vanorio *et al*. 2005; Park *et al*. 2007; Koulakov *et al*. 2009; Zandomeneghi *et al*. 2009). See Lees (2007) for a review of tomographic studies at volcanoes.

Another technique that provides detailed information about wave propagation is the use of seismic arrays. Seismic arrays are dense deployments of seismic stations that provide a fine, local spatio-temporal sampling of the seismic wavefields. These data can be used to estimate the apparent slowness vectors of the wave fronts propagating across the array. Apparent slowness vectors represent the direction and velocity of seismic waves, and can be used to identify the different components contributing to the wavefield. For example, La Rocca *et al*. (2001) analysed the wavefields recorded by a seismic array at Vesuvius volcano, Italy, and found evidences

of waves scattered at the main topographical discontinuities. Almendros *et al.* (2002) used seismic arrays to perform wavefield decomposition at Kilauea volcano, Hawaii. They found different wave components related to source processes, surface waves and scattering at the main discontinuities of the medium.

In some situations, array analyses permit the detection of seismic wave propagation anomalies. In this context, the word 'anomaly' means an observation that cannot be explained using simple velocity models, i.e. laterally homogeneous media. The use of multiple array deployments and/or active sources is adequate to understand the effect of the medium. For example, Saccorotti *et al.* (2001) detected slowness vector anomalies at Deception Island volcano (Antarctica). They found inconsistencies between the apparent slowness vectors of regional earthquakes recorded at two different seismic antennas. They interpreted these discrepancies in terms of the effect of a sharp lateral velocity contrast. Saccorotti *et al.* (2004) performed a study of volcanic tremor at Etna using two seismic arrays. The joint interpretation of slowness vector data suggested a strong bending of the seismic rays. They associated this bending to lateral heterogeneity and/or strong topographic effects. Almendros *et al.* (2007) analysed volcanic tremor at Las Cañadas caldera (Tenerife) using three seismic arrays. The inconsistency among simultaneous estimates of apparent slowness vectors suggests a complex wavefield, and prevented them to determine the tremor source location. Nisii *et al.* (2007) analysed shot data recorded by a seismic antenna deployed at Campi Flegrei during the TOMOVES active source survey. They detected systematic discrepancies between the observed and expected values of apparent slowness and backazimuth. They related these differences to the complexity of the velocity structure.

In the present work we analyse data recorded by a multi-array deployment during an active-source tomography experiment carried out in 2005 January at Deception Island volcano (Antarctica). In this experiment, several thousand shots were recorded by eight seismic antennas deployed along the inner coast of the flooded caldera of Deception. Since the positions of the seismic sources and receivers are accurately known, the analysis of the observed ray parameters allows us to investigate the effect of the heterogeneous medium in the propagation of the seismic waves.

2 GEOLOGICAL AND GEOPHYSICAL SETTING

Deception Island is an active strato-volcano located at the southwest end of the Bransfield Strait, a backarc basin that developed between the South Shetland Islands and the Antarctic Peninsula (Fig. 1). The South Shetland Islands formed as the result of the subduction of the Phoenix plate beneath the Antarctic plate. The rate of subduction decreased dramatically at about ∼4 Ma (Barker 1982) and continues today, if at all, only very slowly (Robertson-Maurice *et al.*, 2003).

Deception Island lies at the boundary between the Central and Western Bransfield Basins and its footprint extends from the northeastern boundary of the basin to the axis of backarc extension. The emerged top of the volcano is a small horseshoe-shaped island with a diameter of ∼15 km that encircles a flooded caldera, named Port Foster, with a narrow opening to the sea. Most of the island is covered by glaciers, cones and lava flows. The volcanic activity extends from 0.75 Ma to the last eruptions in 1842, 1967, 1969 and 1970 (e.g. Baker *et al.* 1975, Smellie 2001).

Deception Island has traditionally been considered a collapse caldera (Baker *et al.* 1975), although extensive deposits from the caldera-forming eruption have yet to be identified. Martí *et al.*

(1996) interpreted fault patterns around the caldera in terms of an alternative model in which the caldera formed as a passive response to regional extension. More recently, Smellie (2001) re-interpreted the lithostratigraphy of Deception Island and proposed a model in which mixing of two magma types lead to an explosive eruption with collapse occurring on intersecting faults that had been formed by regional extension. The main fault directions are NE–SW (parallel to the Bransfield extension), NW–SE and NNW–SSE, among others (De Rosa *et al.* 1995; Rey *et al.* 1997, 2002; González-Casado *et al.* 1999; Paredes *et al.* 2006; Carmona *et al.* 2010). Deception Island seismicity includes volcano-tectonic earthquakes related to the activation of these sets of faults, as well as long-period seismicity mostly related to the interactions between shallow aquifers and hot materials (Almendros *et al.* 1997, 1999; Ortiz *et al.* 1997; Alguacil *et al.* 1999; Ibáñez *et al.* 2000, 2003).

Many seismic studies have demonstrated the complexity of the structure of Deception Island volcano. For example, Vila *et al.* (1995) observed low velocities of the seismic waves across Port Foster. They related these delays to the presence of a low velocity body. Saccorotti *et al.* (2001) estimated the shallow velocity structure at two sites, obtaining very different results. These differences were responsible of a strong bending of the ray paths from regional earthquakes. Luzón *et al.* (2010) have completed this study sampling nine sites around Port Foster. They obtain a variety of velocity models that show important differences, even for nearby sites. Recently, Ben-Zvi *et al.* (2009) and Zandomeneghi *et al.* (2009) have performed active source seismic tomography inversions in 2-D and 3-D, respectively. The main feature of the tomographic images of Deception Island is the presence of a low-velocity, shallow magma chamber under Port Foster, surrounded by high-velocity chilled magmatic bodies.

3 INSTRUMENTS AND DATA

The instruments and data we analyse are part of the TOMODEC experiment, carried out at Deception Island in 2005 January as an international effort led by University of Granada, Spain. This experiment was designed to obtain a high-resolution, 3-D *P*-wave velocity model of the volcano and surrounding areas (Zandomeneghi *et al.* 2009). It combined a high density of seismometers, both on land and on the seafloor, with an even denser distribution of active sources. The shots were produced by an airgun array fired from the Spanish R/V Hesperides. Within the caldera, we used an airgun capacity of 1500–2000 cu.in., shooting every 60 s (∼150 m) while cruising along a 0.5 km grid (Fig. 2a). We performed two rounds of shooting along similar grids on January 8 and 16, which allowed us to redeploy part of the instruments and improve the coverage. Each shooting leg took over 10 hr, and produced around 600 shots.

We analyse the first arrivals of shot seismic data recorded by eight seismic arrays deployed at the most accessible sites around Port Foster during the TOMODEC experiment. Fig. 2 shows the array locations, configurations and beam-forming responses. Array apertures ranged from 0.2 to 1.3 km. Arrays M, F, J and H recorded the shots fired in the first leg, while arrays E, K, G and L recorded the shots fired in the second leg. The twelve array channels available were connected by cable to up to 11 vertical-component seismometers and one (optional) three-component seismometer. All receivers were Mark Products L28 instruments, with natural frequency of 4.5 Hz electronically extended to 1 Hz. A data acquisition system sampled these channels in continuous mode at 100 sps with a 24-bit
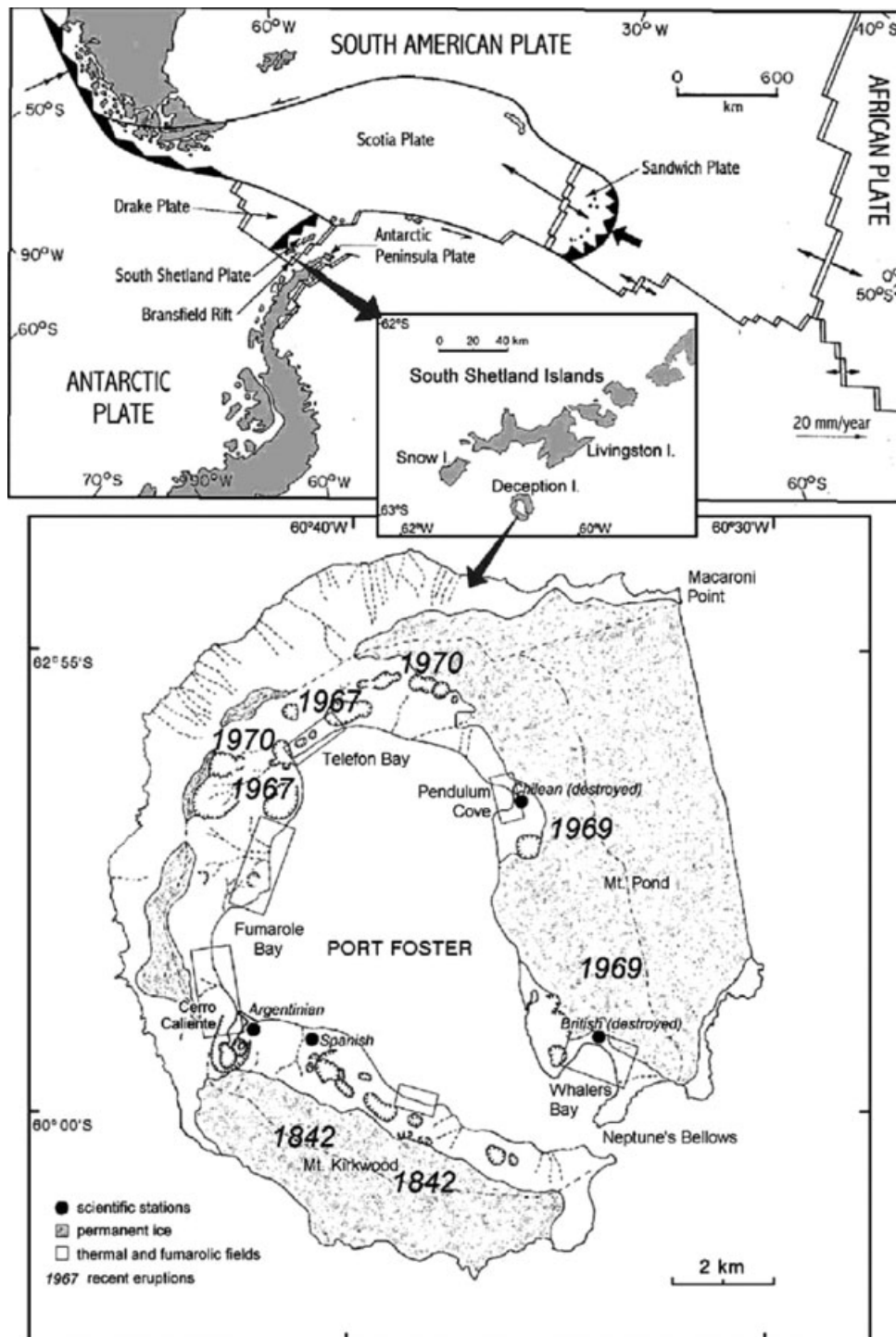
Figure 1. Geological setting of Deception Island volcano, Antarctica. Top panel: tectonic setting of the South Shetland Islands–Antarctic Peninsula region and situation of Deception Island, ∼50 km south of Livingston Island. Bottom panel: map of Deception Island, showing the main volcanic features.

A/D converter, and stored the data into an external hard disk. Absolute timing was obtained using a GPS receiver. See Abril (2007) for a full description of the data acquisition system.

Shot seismograms are characterized by relatively impulsive first arrivals. However, the character of the signals depends on the shot range and also the shot azimuth. This suggests that wave propagation occurs across a highly heterogeneous medium. Traveltimes from source to receiver range between 0.5 and 5 s. Shot records have durations around 10–15 s, and their spectral contents are centred at

∼6 Hz (Fig. 3). Array records show coherent first arrivals (Fig. 4), although the duration of this coherent phase depends strongly on the array aperture.

4 METHOD AND DATA PROCESSING

We have used the Zero Lag Cross Correlation (ZLCC) method (Frankel *et al.* 1991; Del Pezzo *et al.* 1997, Almendros *et al.* 1999) to calculate the apparent slowness vectors of the first arrivals
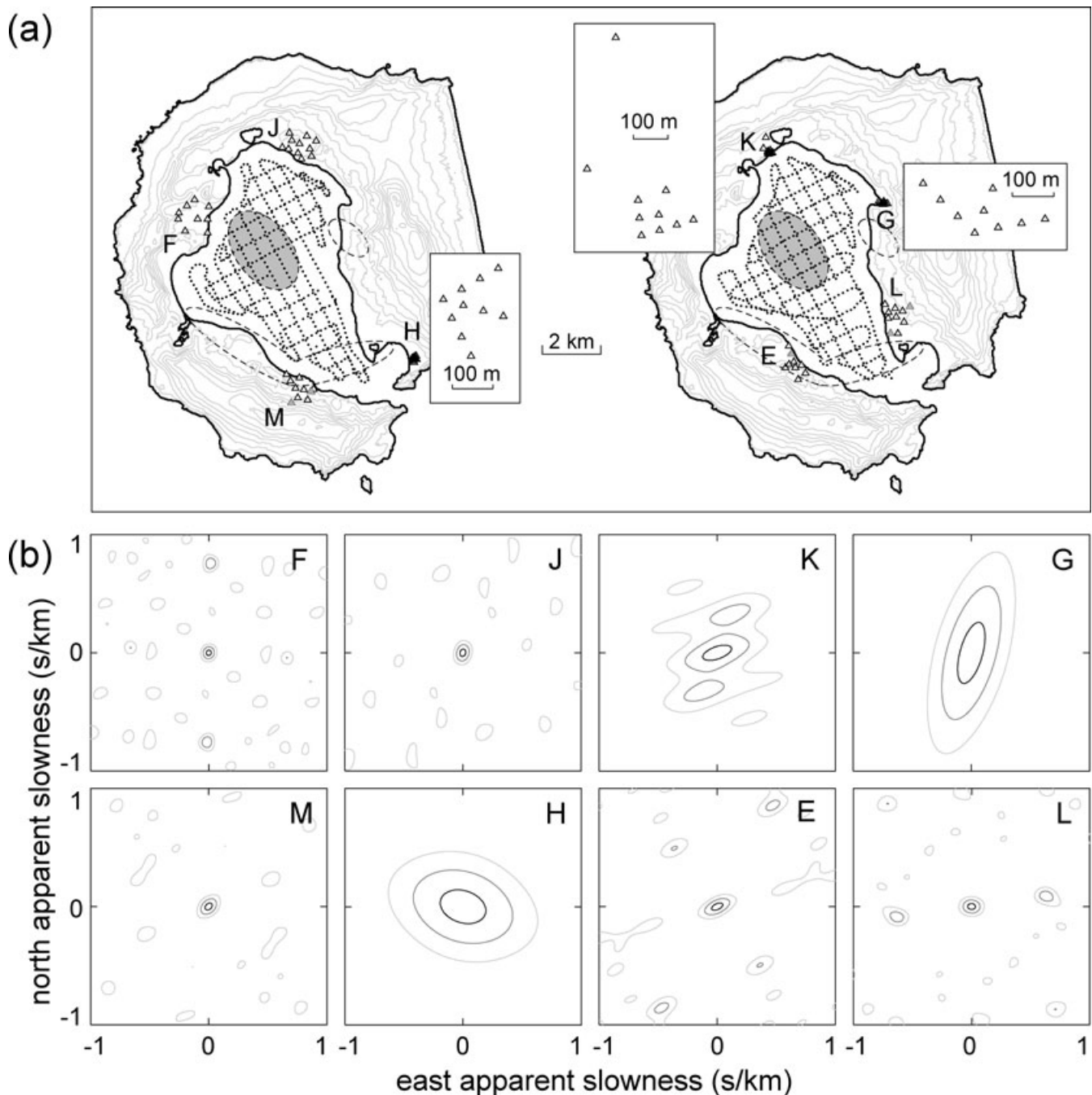
Figure 2. (a) Location and configuration of the arrays used for this work. The left and right maps correspond to the shot and instrument locations used during the first and second legs of the TOMODEC experiment (see text for explanations). The insets show a zoom on the configurations of the small aperture arrays. The dashed areas indicate the main *P*-wave velocity anomalies imaged by Zandomeneghi *et al*. (2009). The grey area is a low-velocity region, while the white areas are high-velocity regions. (b) Beam-forming array responses at 6 Hz for the eight arrays selected, in the slowness range from –1 to 1 s km^{-1} in east and north components.

generated by the airgun shots. The ZLCC technique performs a grid search in the apparent slowness space, intended to maximize the array-average cross-correlation of the aligned waveforms. In this time-domain method, the wave fronts propagating across the array are assimilated to plane wave fronts, that can be represented by their apparent slowness vectors, or alternatively by their propagation azimuths and apparent slownesses.

In order to apply the ZLCC method to array data, we have to select an adequate set of parameters, including the filter, time win-

dow and apparent slowness grid. We used a bandpass, zero-phase Butterworth filter in the 3–15 Hz frequency band, where most of the shot energy is concentrated (Fig. 3). With this filter we reduce the influence of oceanic noise, volcanic tremor and other volcanic signals generally observed at frequencies below 3 Hz (Ibáñez *et al*. 2000, 2003). We also eliminate other sources of high-frequency noise such as wind, human activities, etc. We selected a window length of 0.4 s (40 samples) for the correlation analyses. This window represents about 2.5 periods at the dominant frequency of 6 Hz,

2005-01-08 07:21:15.0
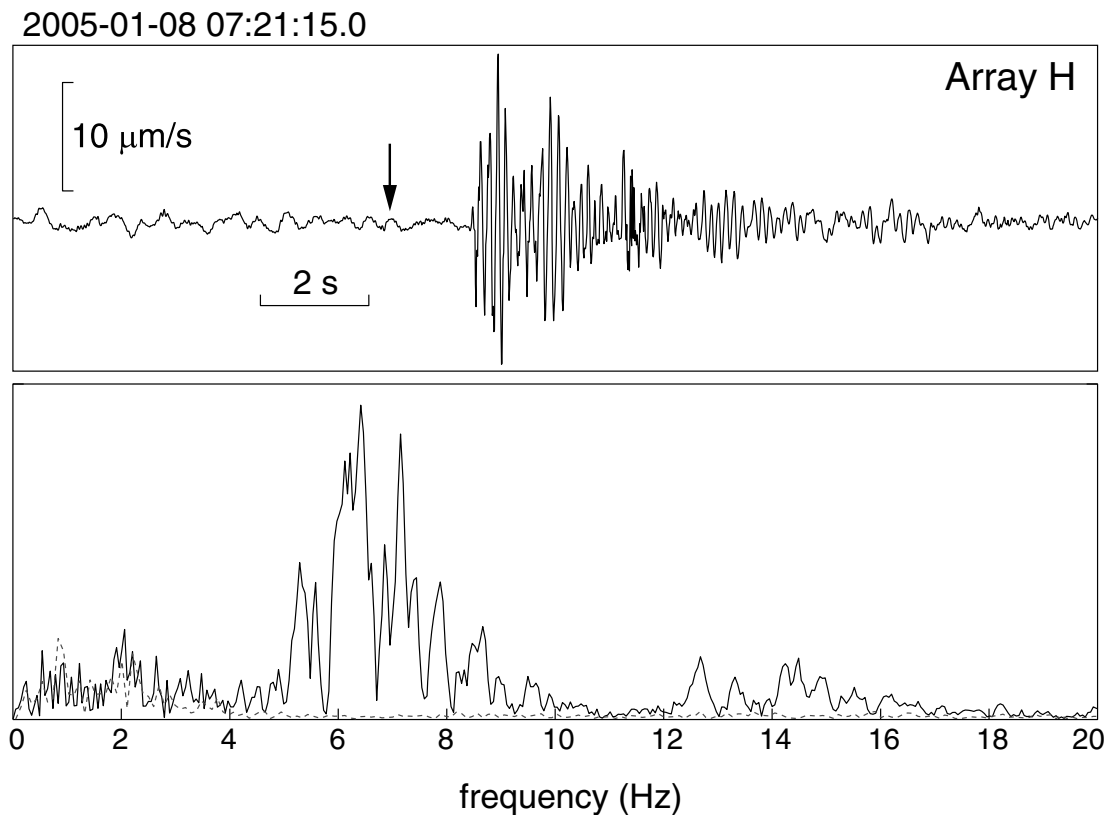
Figure 3. Top panel: raw seismogram of a shot recorded at array H. The time displayed at the top corresponds to the start of the window shown. The shot time is indicated by a vertical arrow. It was fired at 2.9 km NW of the array site. Bottom panel: Amplitude spectra of the signal (solid line) and noise (dashed line).

which has been suggested as the optimum window length for this type of analysis (Almendros *et al.* 1999). The size and spacing of the apparent slowness grid have to be chosen carefully, having into account the expected range of apparent slowness, array configuration and sampling rate. We assumed that first arrivals are composed of body waves propagating from the source to the array along relatively shallow paths. For these waves, we cannot expect arrivals with apparent slowness larger than the slowness of the shallowest layer, which in most models of Deception Island is smaller than 1 s km^{-1}. Thus, we took a range of –1 to 1 s km^{-1} for the East and North components of the apparent slowness vector. The optimum grid interval has to provide at least a delay of one sample between the shot arrivals recorded at the most distant stations of the array. Theoretically, the minimum grid interval can be estimated as $\Delta s = \Delta t / D$, where Δt is the sampling interval of 0.01 s and D is the array aperture. For the small- and large-aperture arrays, the average apertures are about 0.35 and 1.1 km, respectively, which implies optimum apparent slowness grid intervals of 0.025 and 0.01 s km^{-1}.

We calculated the array-averaged cross-correlation for the selected array data at all the apparent slowness grid nodes, using the apparent slowness vector defined by the node to correct the waveform delays. The position of the node where the maximum average cross-correlation (MACC) is reached provides an estimate of the apparent slowness and azimuth of the incoming wave fronts. The region in the apparent slowness space with average cross-correlations above 90 per cent of the maximum provides an estimate of the uncertainty of the solution. The sizes and shapes of these regions are related to the array configurations. In Fig. 2(b) we show the beamforming array responses at 6 Hz for the selected arrays. Large

aperture arrays generally display a narrow main peak, although there are relatively important secondary peaks produced by spatial aliasing. Small-aperture arrays show wider peaks, resulting in lower resolution and larger uncertainties.

We repeated these operations along the seismograms by shifting the selected time window by a 10 per cent of its duration (four samples). In this way, we obtain time series of apparent slowness, azimuth and MACC for the whole shooting period.

In order to assign unique apparent slowness and propagation azimuth to each shot at each array, we analysed the results in a temporal window around the *P*-wave arrival (Fig. 5). We selected the best solutions based on these criteria: (1) temporal proximity to the first arrival of the shot records; (2) occurrence of a correlation peak with a correlation value larger than twice the noise correlation; (3) small uncertainties in the apparent slowness and azimuth estimates and (4) stability of the solutions in apparent slowness and azimuth. The final apparent slowness and azimuth are obtained as a correlation-weighted average of the selected values. To quantify the quality of these estimates, we assign a qualitative factor that represents how well the solution fulfils the above criteria. This quality factor ranges from 1 (for a very good solution matching entirely all the criteria) to 5.

Fig. 5 shows an example of the procedure for two shots at arrays E and H, at ranges of 3.1 and 2.1 km, respectively. The grey windows correspond to the selected interval, where the former criteria are met. Small aperture arrays have larger maximum correlations than large aperture arrays. The number of the stable solutions for azimuth and apparent slowness is generally smaller for large aperture arrays, where correlation decreases faster than for the short aperture arrays.
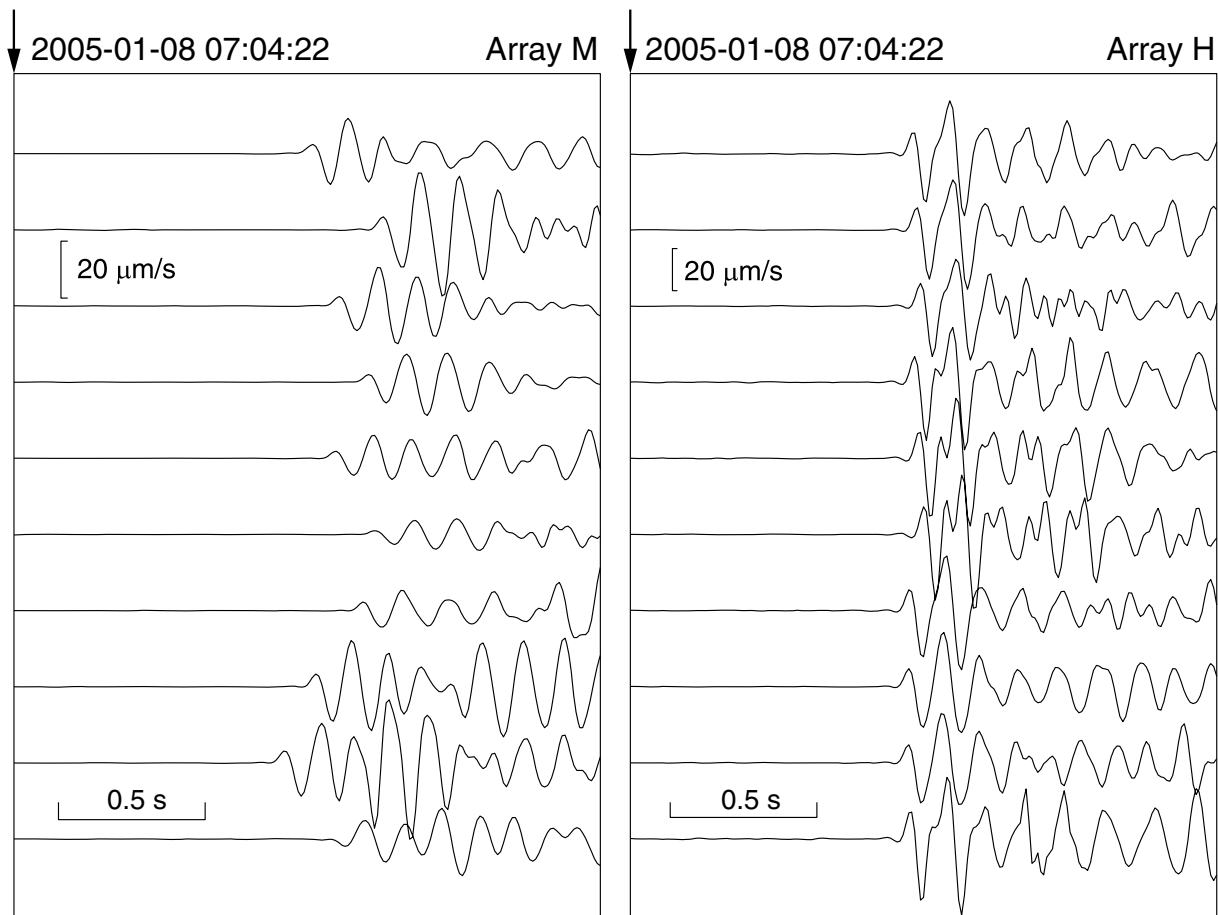
Figure 4. Filtered seismograms (3–15 Hz) showing the *P*-wave arrivals for all channels at arrays M (large aperture, left) and H (small aperture, right) for a single shot located midway between them, at distances of 2.2 and 1.8 km, respectively. The shot time is indicated by an arrow and coincides with the start of the window.

5 RESULTS

The procedure described above allows us to calculate a set of ~5000 slowness vectors that characterize the first arrivals of the shots to the seismic arrays. To extract the most significant solutions among this data set, we consider only those solutions characterized by: (1) quality factors of 1 or 2; (2) maximum average cross-correlations larger than 0.5 and 0.6 for large- and small-aperture arrays, respectively and (3) minimum apparent slownesses of 0.05 and 0.15 s km^{-1} for large- and small-aperture arrays, respectively. These limits represent five to six times the slowness grid interval, which ensures an adequate resolution in azimuth.

Figs 6 and 7 show a summary of the results for six of the seismic arrays. To build these figures we artificially place the propagation parameters estimated by the array (azimuth and apparent slowness) at the corresponding shot locations. These parameters are spatially interpolated to obtain 2-D distributions. We have to mention that interpolation creates some artefacts, especially in those areas with few shots (for example, the bay boundaries). We plot the shot positions to help discriminate the significant areas. Nevertheless, it is very important to keep in mind that the values should not be assigned to the point where they appear. They are not a property of the medium at the shot location, but a result of the interactions of the seismic wavefield and the medium between the shot location and the array.

In Fig. 6 we display the azimuth anomaly, rather than the propagation azimuth itself. For each shot, the azimuth anomaly is defined as the difference between the azimuth estimated by the array, that describes the orientation of the apparent slowness vector, and the geometrical azimuth from the shot position to the array centre. A positive/negative anomaly means a clockwise/counter-clockwise rotation of the observed slowness vector compared to the shot-array direction. For most arrays, we observe the occurrence of large azimuth anomalies (up to 60°) at extended regions of Port Foster. Four areas display significant positive anomalies: the east and northeast limits of Port Foster for array M; the southern limit of the caldera, near Whalers Bay, for array E; the west side of Port Foster for array J and the north half of the bay for array L. Negative anomalies are found mostly at the west side of Port Foster for array E, and at the northernmost limits of the bay for array G.

In Fig. 7 we plot the distributions of apparent slowness. Generally speaking, the most important factor controlling the apparent slowness of the first arrival is the shot-array distance. Nearby shots produce large apparent slowness values above 0.6 s km^{-1}, while distant shots produce small values, down to about 0.15–0.20 s km^{-1}. In terms of apparent velocities, shot arrivals range between 1.5 and 7 km s^{-1}. However, the radial patterns are not identical, and indeed there are important differences among arrays. For example, for similar shot-array distances array G seems to detect arrivals that are always slower than in the remaining arrays, while array M produces the fastest results. Moreover, the apparent slowness variation with shot-array distance for array H is slow, resulting in a quite homogeneous distribution. On the contrary, array E results show
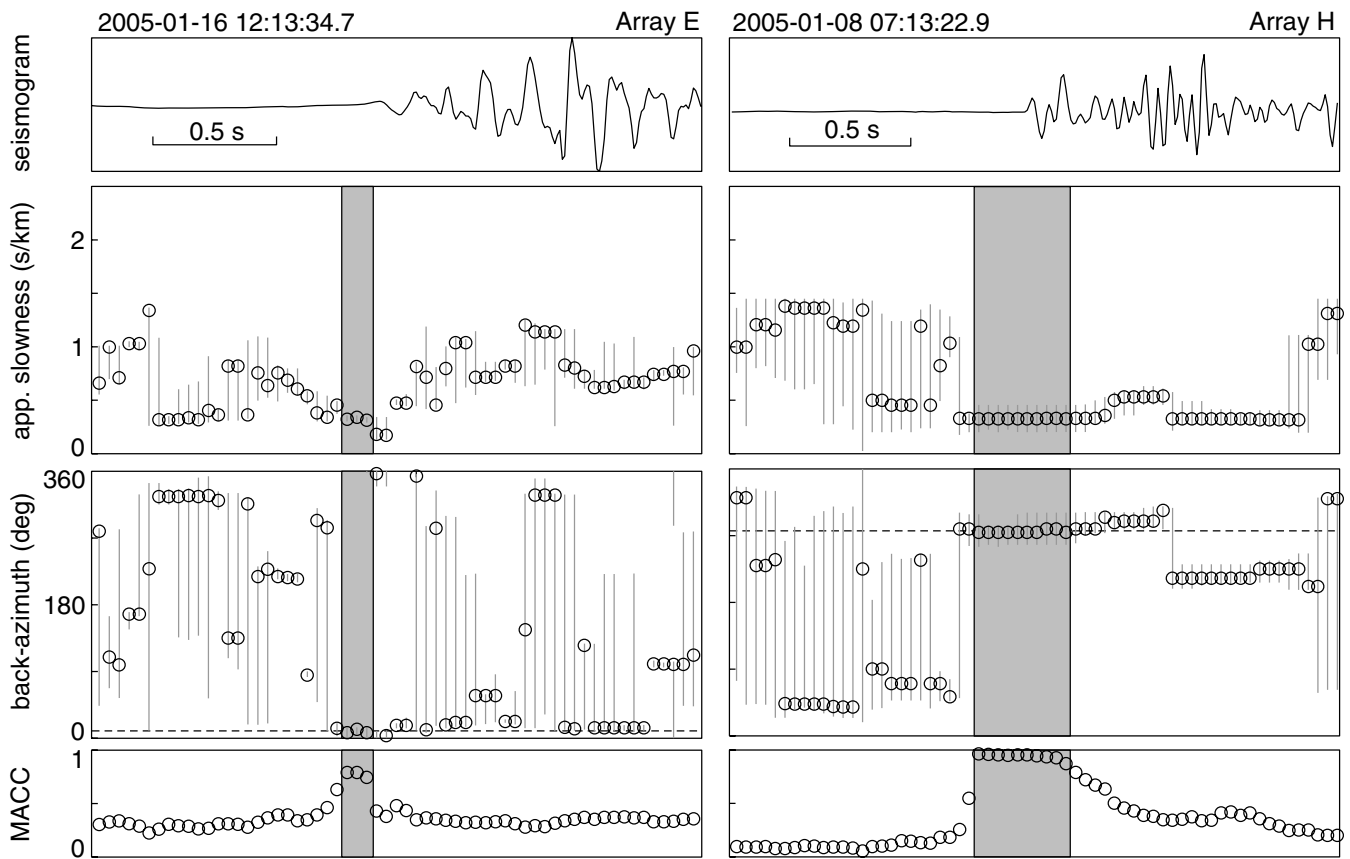
Figure 5. Example of the procedure to determine the propagation parameters of a shot recorded at a seismic array. We show examples from arrays E (large aperture, left-hand panel) and H (small aperture, right-hand panel). The times displayed at the top correspond to the start of the windows shown. Shot times are 12:13:34.06 for array E and 07:13:22.06 for array H. Shot-array distances are 2.7 and 2.1 km, respectively. From top to bottom, we display the seismogram from one of the array channels; apparent slowness; backazimuth and maximum average cross-correlation. In the central panels, vertical bars indicate the uncertainties of the solutions. The dashed lines represent the geometrical array-source directions. The grey areas indicate the solutions selected to perform a weighted average (see text for explanations).

the strongest gradient, containing both the largest and the smallest of the apparent slowness estimates for all the array data.

Results for arrays F and K have been neglected on the base of their internal inconsistence. In several areas, the apparent slowness vector estimates provided by these arrays for nearby explosions are incompatible, either in azimuth or apparent slowness or both. As an example, Fig. 8 shows the results for azimuth anomaly and apparent slowness for array F. A relatively large percentage of the results are inconsistent, showing unrealistic changes in azimuth along the shooting lines and/or exceedingly large apparent slowness values. Shot distances along the shooting lines are just ∼150 m, and it seems very difficult to imagine what mechanism would explain such sharp variations.

6 DISCUSSION

6.1 Quality of the results

In this work we use eight seismic arrays to measure the apparent slowness vectors of the first arrivals generated by airgun shots at Deception Island volcano. The array apertures and configurations affect the resolving capabilities and the quality of the apparent slowness vector estimates. We used large and small arrays, with average apertures of about 1.1 and 0.35 km, respectively. The aperture is

related to the size of the central peak in the response function, while the configuration of the stations influences its shape (Fig. 2b). Large arrays (M, E, F, J and L) have narrow central peaks, although secondary peaks due to spatial aliasing may appear. The small value of the apparent slownesses of the first arrivals ensures that we are choosing the right solutions. On the contrary, small arrays (K, G and H) have wide peaks, but they do not show secondary peaks in the slowness range selected. This produces larger uncertainties in the estimates of apparent slowness and azimuth. This effect can be seen in Fig. 9, where the slowness distributions have more dispersion for arrays G and H, especially for distant shots that reach the array with small values of apparent slowness.

Arrays F and K provide a large percentage of inconsistent solutions (e.g. Fig. 8). The low quality of the estimates could be due to the complexity of the shallow structure beneath the array site. One of the hypotheses behind the application of seismic antennas is the assumption of a common, homogeneous structure under the different array receivers. This ensures that the wave fronts propagating across the array can be considered locally as plane wave fronts represented by an apparent slowness vector. In the case of the array F, located at Obsidians Beach, several studies suggest the existence of a strong lateral velocity contrast in the NW boundary of Port Foster, beneath the array F site. For example, Saccorotti *et al*. (2001) determined the shallow structures under two seismic arrays located, respectively, at Obsidians Beach (the F array site)
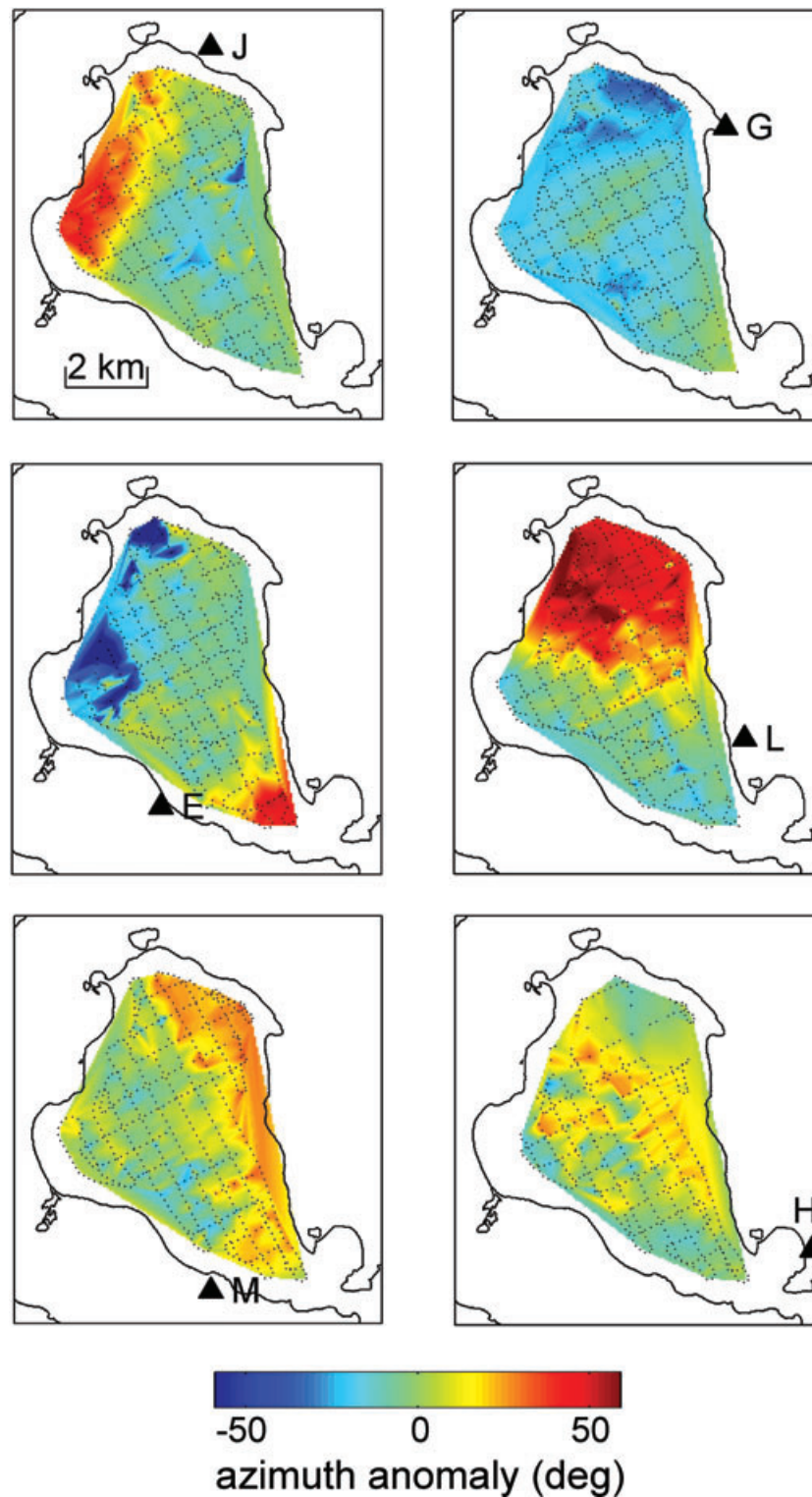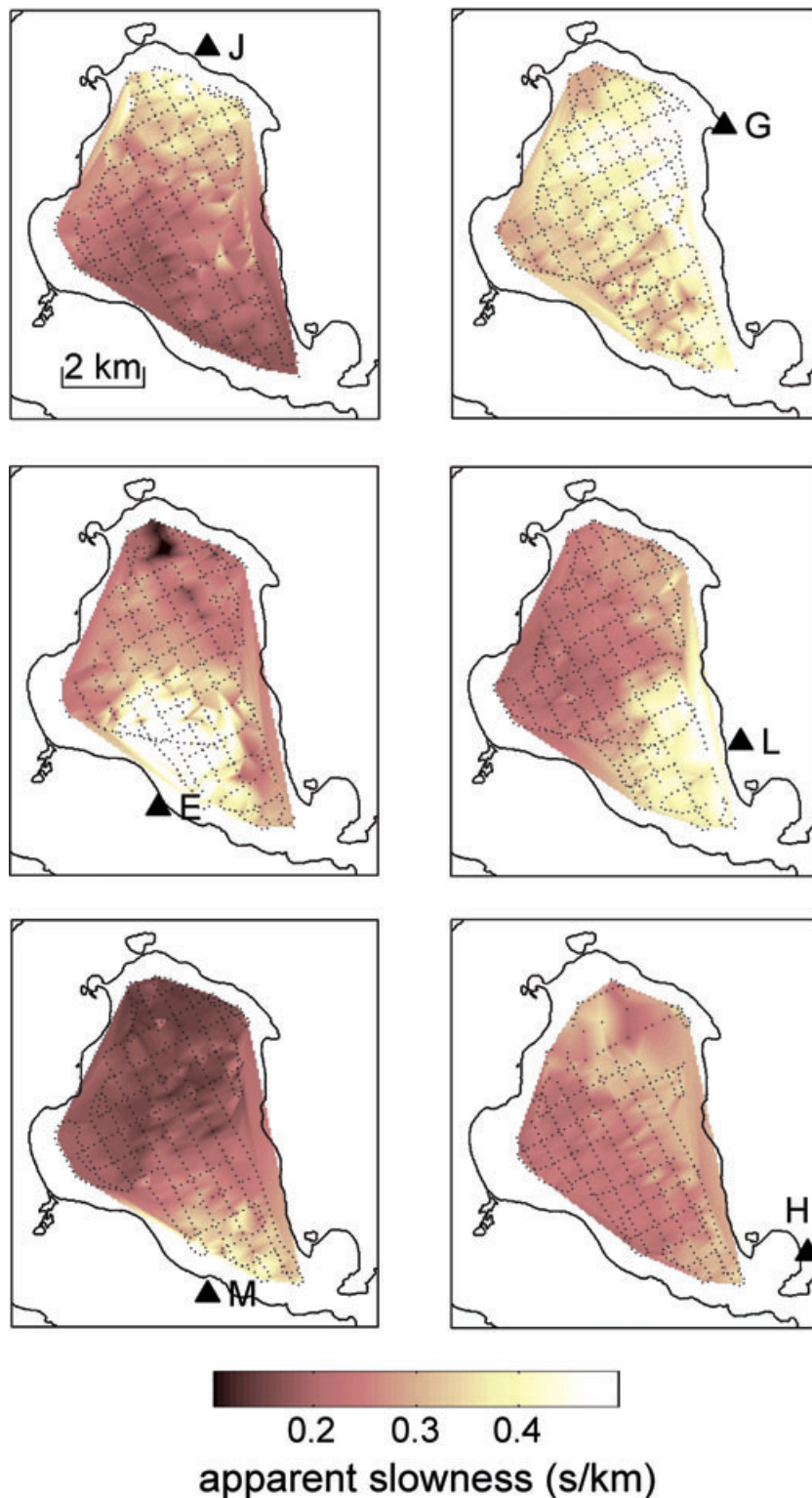
Figure 6. Distributions of azimuth anomalies obtained at the eight arrays. For each shot, we assign the azimuth anomaly measured at the array to the shot location, and interpolate to obtain a 2-D distribution.

and Fumarole Bay, near the Argentinean Station (e.g. Fig. 1). These structures were very different, suggesting the presence of a fracture system between the array sites, perhaps related to caldera formation. Luzón *et al*. (2010) investigated the shallow structure around the Port Foster coastline, using the same instrument layout described in this work. Most arrays were located on structures that could be

modelled using 1-D models. However array F had to be divided into two subarrays to obtain coherent results. The SW stations were deployed on a fast structure that is in concordance with the caldera border. The NE stations were on a slow structure related to post-caldera volcanoclastic deposits. These results are supported by the high-resolution seismic tomography performed by Zandomeneghi
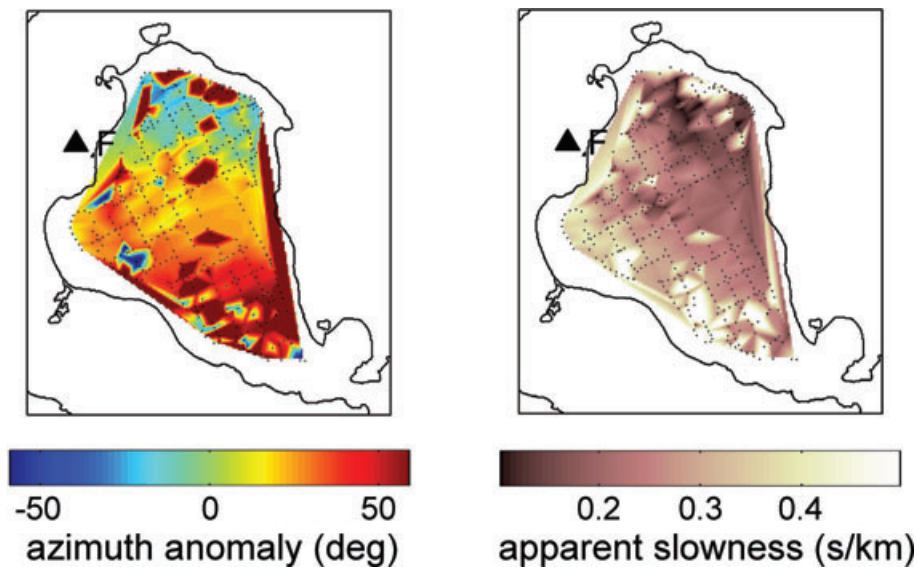
Figure 7. Distributions of apparent slowness obtained at the eight arrays. For each shot, we assign the apparent slowness measured at the array to the shot location, and interpolate to obtain a 2-D distribution.

et al. (2009). The main structural features of the seismic image of Deception Island are a low-velocity volume located under Port Foster and interpreted as a shallow magma chamber, and a high-velocity region NW of Deception, that corresponds to the basement of the South Shetland Islands. Array F was located in the contact between these two features. We believe that the inability of array

F to produce a consistent set of apparent slowness vectors for the shot data is related to wave front distortions induced by this strong lateral heterogeneity.

In the case of the array K, located near Telefon Bay, not far from array F, the inconsistence of the results could be related to a similar effect. However, the array aperture is smaller, which would require

Figure 8. Distributions of azimuth anomalies and apparent slowness obtained for array F.

an even larger horizontal gradient. This area is located among the sites of the 1967 and 1970 eruptions, and is nowadays a water-saturated zone with several lakes and maars. Perhaps the properties of pyroclastic deposits with different degrees of water saturation may induce site effects important enough to reduce the coherence of the first arrivals and distort the wave fronts.

Therefore, only seismic arrays M, E, J, G, L and H are used to assess the apparent slowness vectors distributions. These vectors represent the directions and apparent velocities of the wave fronts propagating across the array sites. They depend primarily on: (1) the shot locations, where the wavefields are produced; (2) the arrays, where the wavefields are recorded and (3) the characteristics of the medium in which the wavefields propagate. In our case, since shot and array locations are known, we are in a fair position to investigate the effect of the medium on seismic wave propagation.

### 6.2 Interpretation of the results

In laterally homogeneous media, seismic rays are contained in a vertical plane that includes the source and the receiver (i.e. the array centre). Thus the expected azimuth anomaly is zero everywhere. Any deviation from zero indicates the presence of lateral heterogeneities that affect the ray path. In the case of apparent slowness, the interpretation is a bit more complex. A laterally homogeneous medium implies a radial distribution of apparent slowness. If the seismic velocity increases with depth, we should observe that apparent slowness decreases with increasing shot-array distance. For example, for a medium with a constant velocity gradient, $v(z) = v_0 + kz$, the apparent slowness can be expressed as a function of distance as $s(x) = [(kx/2)^2 + v_0^2]^{-1/2}$. However in general the expected values of apparent slowness in a laterally homogeneous medium are not known *a priori*, since they depend on the velocities of the different layers of the medium. In any case, the assumption of lateral homogeneity simplifies the problem to a radial distribution of apparent slowness vectors.

Nevertheless, volcanic regions are not laterally homogeneous media. They display strong lateral contrasts with different bodies of low and high velocity, as imaged by seismic tomography studies (e.g. Lees 2007). The seismic wave fronts are affected by these heterogeneities. Seismic waves speed up in high-velocity regions

and slow down in low-velocity areas, producing distorted wave fronts and twisted ray paths. For example, to fix ideas, let us assume the presence of a low-velocity body (i.e. a magma chamber) located between the source and the receiver. Seismic rays would follow the fastest paths, turning around (instead of across) the low-velocity body. The rays would not necessarily be contained in a vertical plane. In terms of azimuth, this implies that the wave fronts would reach the array with a propagation azimuth different from the source-array direction. Looking from the receiver to the low-velocity body, those sources located to the right of the low-velocity zone would have a positive azimuth anomaly, while those to the left would have a negative anomaly. Apparent slownesses tend to be smaller, since the rays will penetrate deeper to avoid the low-velocity region. If we have a high-velocity region between the source and the array, we expect that the sign of the azimuth anomaly is opposite to the low-velocity case; and that the apparent slowness gets larger, indicating shallower ray paths.

However, the interpretation in real situations can be much harder. Real volcano structures usually combine depth-dependent velocity gradients, low-velocity regions related to partial melt and/or hydrothermal alterations, and high-velocity regions usually interpreted as chilled magma bodies. On top of this, we must keep in mind the effects produced by the sharp topography of volcanic areas and the presence of strong scatterers and attenuating bodies (Neuberg and Pointer 2000; Martínez-Arévalo *et al*. 2003, 2005; Tramelli *et al*. 2006, 2009; Del Pezzo 2008; Métaxian *et al*. 2009; O'Brien and Bean 2009). Therefore, it is very difficult to estimate precisely what values of azimuth and apparent slowness should be expected for seismic waves propagating in heterogeneous media.

In the case of Deception Island, we have a horseshoe-shaped island with a complex velocity distribution. Seismic images of Deception Island volcano obtained by seismic tomography (Zandomeneghi *et al*. 2009) show the presence of different high- and low-velocity volumes related to the volcano structure. The dominant feature is an elongated low-velocity region located at shallow depths (0.5–5 km) under Port Foster. It is elongated in NW–SE direction with a size of roughly 5 × 2 km. The centre of the anomaly is a bit offset towards the NW. It has been interpreted as a shallow magma reservoir (Ben-Zvi *et al*. 2009; Zandomeneghi *et al*. 2009). Smaller high-velocity regions surround the inner bay along the coastline in
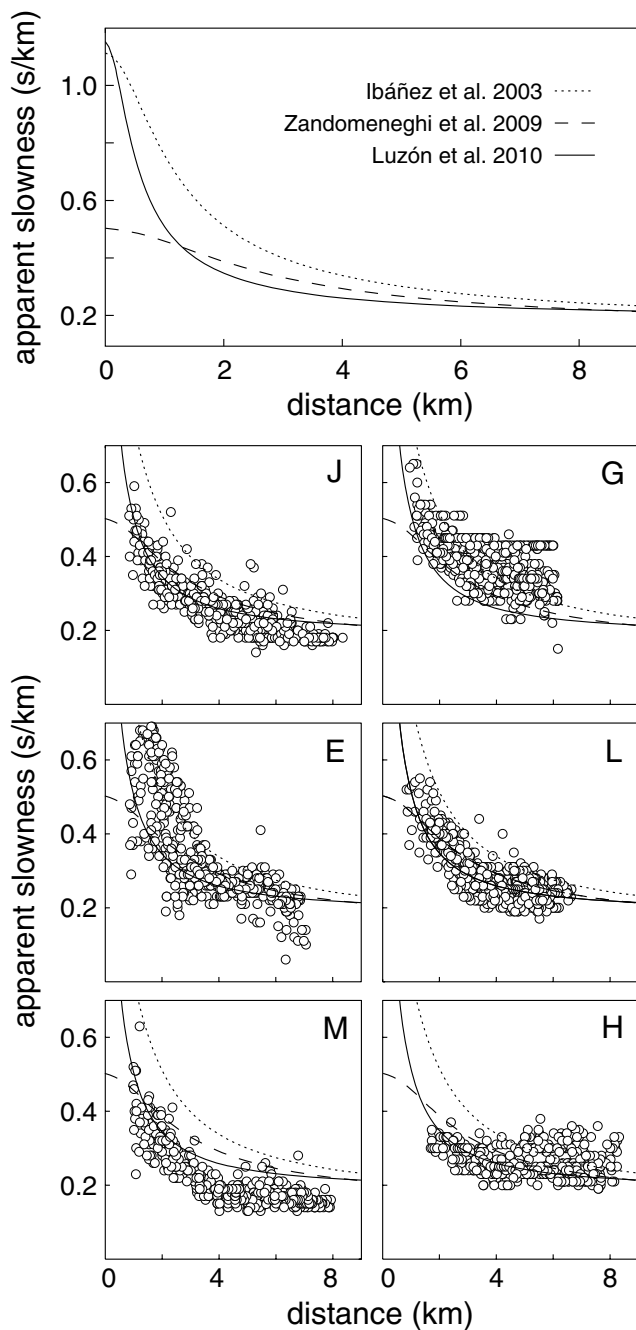
Figure 9. Top panel: apparent slowness calculated as a function of distance for different models of Deception Island volcano. Bottom panel: apparent slowness measured at the seismic arrays, plotted against the shot-array distance.

the NE and S–SW sides, related to the ancient caldera structure. The NE anomaly is located near Pendulum Cove, and extends to about 2.5 km in depth. The S–SW anomaly follows the shape of the caldera from Neptune's Bellows to Fumarole Bay. In this case, the anomaly extends deeper and merges with another high-velocity anomaly located south of Deception Island.

Apart from these evidences about the highly heterogeneous structure of Deception Island volcano, we have to underline that we are using data provided by an active seismic experiment. Thus we are dealing with high-frequency, very shallow sources. In this sense, our apparent slowness estimates from the TOMODEC data set may

constitute an extreme situation. In general, high-frequency seismic waves are affected by topography and the heterogeneous structure more than low-frequency waves, due to the reduced wavelengths. Moreover, the shallow structure is expected to be more heterogeneous. Deeper sources should provide a better agreement between expected and observed apparent slowness vectors since the rays sample a more homogeneous medium.

In the following, we discuss the apparent slowness vector distributions in terms of propagation azimuth and apparent slowness.

6.2.1 Propagation azimuth

Although many of the azimuth estimates are in concordance with the apparent slowness vectors expected for a layered medium, there are also noticeable differences. We identify several regions where the shots produce wave fronts that propagate across the array sites in directions quite different from the shot-array directions. In these cases, the medium plays indeed a crucial role in wave propagation. Similar azimuth anomalies of up to 50° have been observed by Nisii *et al.* (2007), who performed a detailed study of wave propagation in the Campi Flegrei area during the TOMOVES experiment using both source and receiver arrays. Almendros *et al.* (2001b) also detected large azimuth anomalies of tens of degrees during the analysis of long-period seismicity at Kilauea volcano (Hawaii) using three seismic arrays. Finally, La Rocca *et al.* (2008) found backazimuth differences of up to 20° between network and array locations of earthquakes in the Cascadia subduction zone.

Some details of the azimuth distributions could be explained by the presence of a magma chamber under Port Foster. In some cases the observed patterns of azimuth anomalies (Fig. 6) are similar to the expected pattern for a low-velocity anomaly, described above. This pattern is found for example for arrays J and E. For these arrays, the shots to the right of the centre of Port Foster (looking from the array) display positive anomalies while the shots to the left show negative anomalies. This observation could constitute a confirmation of the presence of a low velocity body under Port Foster. However, although this positive–negative pattern corresponding to a low-velocity body constitutes an interesting first approximation, it does not completely explain the observed features.

In fact, although most areas of positive azimuth anomaly are found in the proper position, to the right of the bay centre looking from the array, some cases do not display a negative anomaly region that should be there by symmetry if the only effect was the presence of a low-velocity body under Port Foster. Although the shot coverage is not symmetric either, having more shots at one side than the other, in general areas of positive anomaly are more marked and extended than the negative anomalies. For example, array L displays a large positive anomaly filling the north half of the bay. There is almost no trace of negative anomalies to the south of the bay. Another discrepancy is related to the position and extent of the magma chamber. This chamber is located at the centre of Port Foster, and it is elongated in a NW direction extending from the bay centre to the shoreline of Obsidian Beach. At array E, the red-blue pattern extends to the south even further than the chamber limits. We could only explain the red patch in Fig. 6 by assuming a much larger magma chamber extending also from the centre of the bay to the south, which has not been imaged by seismic tomography (Zandomeneghi *et al.* 2009).

Therefore, there must be more structures affecting wave front propagation. For example, high velocity bodies surrounding Port Foster may contribute to the distortion of the simple magma chamber

pattern. The positive anomalies observed at the southernmost shots for array E could be related to a high velocity region along the southern shoreline of Port Foster, rather than to the central magma chamber. Given the positions of the anomalous bodies, the effect of both adds in the same sense, producing a strong positive anomaly in the area (Fig. 6).

The only case where we find negative anomalies to the right of the magma chamber is for array G. In this case, there are no positive anomalies in the analysed area. We think that a nearby (<1 km) high-velocity body located to the south of array G (Zandomeneghi *et al.* 2009) can be responsible for this effect. The fastest seismic rays would be those passing through this high-velocity area. Looking from the array to the high-velocity centre, most shots fall to the right, and therefore, they arrive to the array with negative azimuth anomalies (as described above for a high-velocity body).

6.2.2 Apparent slowness

As for the apparent slowness, the results show basically radial distributions. Fig. 9 shows a representation of the apparent slowness results as a function of shot-array distance for the six arrays. We also include for comparison the apparent slowness values expected for several 1-D earth models used for Deception Island. In a laterally homogeneous medium, the velocity structure would be the same for all arrays. Therefore, the radial patterns should be identical. We can see that results for arrays J, L and H are consistent and fit reasonably well the Luzón *et al.* (2010) average model. The apparent homogeneity of the array H results, with values limited to the range 0.2–0.4 s km^{-1}, can be an artefact due to the relatively large distances from the array to the closest shots.

However, we observe significant differences in the radial patterns for other arrays. Array E has a sharp apparent slowness gradient, especially for close shots, that seems to be anomalous. If we compare these results with the arrays J or L, we find larger apparent slownesses at larger distances. This discrepancy could be explained by the presence of a high-velocity body near array E (Zandomeneghi *et al.* 2009). This body would force seismic rays to become shallower, and therefore the incidences would be more horizontal and the apparent slownesses larger. This high-velocity anomaly was also invoked to explain the origin of the positive azimuth anomaly.

Another intriguing result refers to the absolute value of the apparent slowness. Most arrays have values around the results expected for the Luzón *et al.* (2010) model. However, array G has generally large apparent slowness values, while array M has small values. In the case of array G, this result is in agreement with the presence of a shallow, nearby high-velocity body, as suggested above to explain the observed azimuth anomalies. A shallow high-velocity anomaly makes the seismic rays to travel at shallower depths, thus arriving at the array site with higher apparent slownesses.

Finally, although as a first approximation the apparent slowness patterns fit to radial distributions, there are some azimuthal variations as well (Fig. 7). For shots located at similar distances from the array, the estimates of apparent slowness show different values. Although this effect can be detected for all arrays, it is especially evident for arrays M, E, L and H. These azimuthal variations of apparent slowness must be related to an important lateral heterogeneity of the velocity structure. For example, for array E some shots located near the north coast of Port Foster show anomalous values of apparent slowness, which are smaller than for nearby shots located at similar distances. This could be explained by the presence of a low-velocity region at the centre of the bay. Seismic rays

from the north half of Port Foster would penetrate deeper and arrive to the array with low apparent slownesses. However the limited spatial extent of this area of small apparent slowness implies that the low-velocity region should be smaller than the body imaged by Zandomeneghi *et al.* (2009) and sketched in Fig. 2.

In general, the azimuth anomalies and apparent slowness variations observed in our analyses cannot be easily explained by simple, qualitative models. The complete interpretation of the apparent slowness vectors observed is a challenging task. We have to take into account other effects such as the local structure of the site in which the array is deployed (Luzón *et al.* 2010), which can strongly affect wave propagation. The topography and bathymetry of Deception Island can also introduce important distortions in the wave fronts. These effects can only be addressed by computer simulations using numerical methods that allow for the resolution of the complete wave propagation problem.

6.3 Future work

In this work, we have assessed the effects of lateral heterogeneities on wave propagation. The results underscore the importance of the path effects and demonstrate the need for the use of accurate seismic models and methods in volcanic areas. Traditionally, the heterogeneity of the velocity structure of volcanoes has been purposefully overlooked in order to apply the classical methods of seismology to volcanic areas. For example, flat-earth models, although unrealistic, have been and are still used to obtain a general view of the volcanic earthquake locations. The simplicity and efficiency of the calculations (that allow for example for real-time source locations) justify the precision drop induced by the use of these simplistic models.

Nevertheless, there is an increasing body of knowledge about the velocity structure of volcanic areas, including digital elevation models to represent the topography and 3-D high-resolution seismic tomography models. Moreover, we have the computational methods and power to reproduce the behaviour of seismic wavefields in complex media (e.g. Ohminato and Chouet 1997; Neuberg and Pointer 2000; Almendros *et al.* 2001a; Ripperger *et al.* 2003; Métaxian *et al.* 2009; O'Brien and Bean 2009).

A direct consequence of our results is that if we want to gather an optimum understanding of seismo-volcanic sources (locations, sizes, mechanisms, etc.) we should review the seismological methods and algorithms to include the effect of the heterogeneities of the medium in wave propagation. This is especially critical for seismic array methods that depend on estimates of apparent slowness vectors. These vectors are very sensitive to the velocity structure, and a simplistic interpretation may introduce important uncertainties. Several authors have successfully addressed this problem using numerical simulations (e.g. Almendros *et al.* 2001a, b; Métaxian *et al.* 2002; Jousset *et al.* 2003). These simulations allow us to understand the effect of the topography and other lateral velocity heterogeneities on seismic wave propagation.

As an example, we have performed several tests to simulate the effects of the medium heterogeneities on the propagating wave fronts at Deception Island. We use the finite-difference method of Ohminato and Chouet (1997) on a 10 × 10 × 5 km volume sampled with a grid cell size of 50 m. The model includes the topography of both the free surface and seafloor. *P*-wave velocities are obtained from the 3-D tomographic model of Zandomeneghi *et al.* (2009). We assume a constant density of 2.65 g cm^{-3}, and a constant Poisson ratio of 0.25. Due to the constraints of the methodology, we compute the wavefield for a 1 Hz source. Fig. 10 shows an example of the
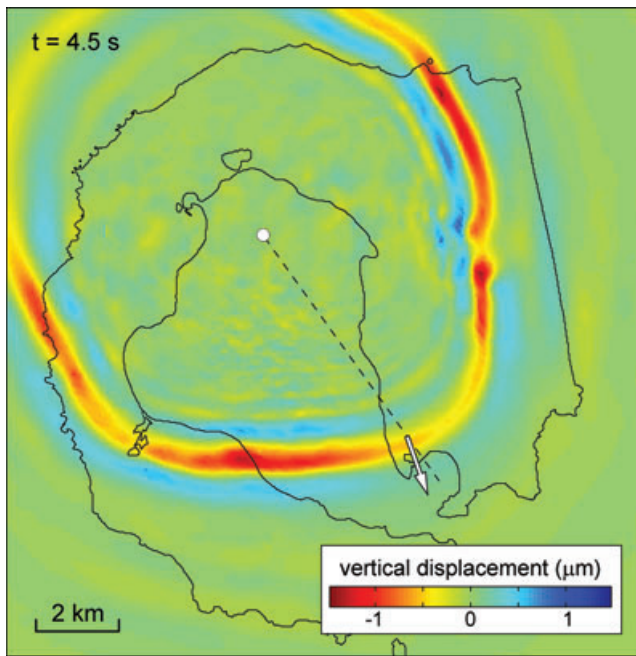
Figure 10. Snapshot of wave propagation through a model of Deception Island volcano that includes topography and 3-D velocity structure. The source is a shallow, 1 Hz, isotropic source located under the north sector of Port Foster. The arrow indicates the direction of the apparent slowness vector of the synthetic wave front at the L array site.

results, corresponding to the wavefield at 4.5 s for a shallow isotropic source located under the northern sector of Port Foster. Instead of the radial symmetry expected for a laterally homogeneous (isotropic) medium, we observe that seismic energy propagates faster in some directions, and focuses in particular regions. These effects produce rather asymmetric wave fronts. To quantify the amount of wave front distortion, we calculate the slowness vector using a synthetic array, that is, a set of spatially separated synthetic seismograms (Almendros *et al*. 2001a). In this case, we use a synthetic array simulating the location and configuration of the L array. As can be observed, the estimated azimuth does not correspond to the shot-array direction, but it is rotated clockwise by about 20°. This represents a positive azimuth anomaly, which coincides with the observations (e.g. Fig. 6). In this case, wave front distortions are basically produced by the presence of a low velocity region beneath the caldera, which has been interpreted as a shallow magma chamber (Zandomeneghi *et al*. 2009). The wave fronts move slower to the south (across the magma chamber) than to the southeast. Thus, the initially circular wave fronts become flat in this direction. These results are the inspiration of a work in progress where we try to reproduce the observed distributions of slowness vectors using a more detailed numerical modelling that might overcome the limitations of the present simulations.

Our results open yet another interesting line of research. Seismic tomography obtains the properties of the medium (e.g. *P*-wave velocity) by inversion of a large number of measures of an observable (e.g. *P*-wave traveltime) generated along the ray paths between many sources and/or many stations. In our case, we have estimated a large number of apparent slowness vectors, corresponding to the propagation of seismic waves from a large set of sources to six seismic arrays. Therefore, we could use our observations to perform a slowness vector tomography of Deception Island caldera. In other words, we could use the slowness vectors as the observable to com-

pare between data and synthetics obtained in a perturbed model. Slowness vectors are highly sensitive to the velocity gradient, so that a slowness vector tomography would be most adequate to define the sizes and shapes of the velocity heterogeneities (Hu *et al*. 1994; Nisii *et al*. 2007). Moreover, ray coverage can be further improved using clusters of sources as seismic arrays. This is the basis of the double-beam method (Kruger *et al*. 1996; Nisii *et al*. 2007), which allows the measure of reversed, receiver-to-source apparent slowness vectors. Of course, several questions arise, such as the need to develop fast and accurate ray tracers that could provide the apparent slowness vectors expected for a particular model, or the need to consider both azimuth and apparent slowness (a vector observable, instead of a scalar). However given the dense source and receiver distributions, we believe that the TOMODEC experiment constitutes an ideal data set to test the feasibility of slowness vector tomography.

REFERENCES

Abril, M., 2007. Evolución, diseño y desarrollo de antenas sísmicas. Las antenas del Gran Sasso, del Vesubio, y las nuevas antenas sísmicas portátiles del Instituto Andaluz de Geofísica. Aplicación a zonas tectónicas y volcánicas, *PhD thesis*, University of Granada (in Spanish).

Alguacil, G., Almendros, J., Del Pezzo, E., García, A., Ibanez, J.M., La Rocca, M., Morales, J. & Ortiz, R., 1999. Observations of volcanic earthquakes and tremor at Deception Island, Antarctica, *Annali di Geofisica,* **42,** 417–436.

Almendros, J., Chouet, B. & Dawson, P., 2001a. Spatial extent of a hydrothermal system at Kilauea Volcano, Hawaii, determined from array analyses of shallow long-period seismicity, 1. Method, *J. geophys. Res.,* **106,** 13 565–13 580.

Almendros, J., Chouet, B. & Dawson, P., 2001b. Spatial extent of a hydrothermal system at Kilauea Volcano, Hawaii, determined from array analyses of shallow long-period seismicity, 2. Results, *J. geophys. Res.,* **106,** 13 581–13 597.

Almendros, J., Chouet, B., Dawson, P. & Huber, C., 2002. Mapping the sources of the seismic wavefield at Kilauea volcano, Hawaii, using data recorded on multiple seismic antennas, *Bull. seism. Soc. Am.,* **92,** 2333–2351.

Almendros, J., Ibáñez, J.M., Alguacil, G. & Del Pezzo, E., 1999. Array analysis using circular wave-front geometry: an application to locate the nearby seísmo-volcanic source, *Geophys. J. Int.,* **136,** 159–170.

Almendros, J., Ibañez, J.M., Alguacil, G., Del Pezzo, E. & Ortiz, R., 1997. Array tracking of the volcanic tremor source at Deception Island, Antarctica, *Geophys. Res. Lett.,* **24,** 3069–3072.

Almendros, J., Ibáñez, J.M., Carmona, E. & Zandomeneghi, D., 2007. Array analyses of volcanic earthquakes and tremor recorded at Las Cañadas caldera (Tenerife Island, Spain) during the 2004 seismic activation of Teide volcano, *J. Volc. Geotherm. Res.,* **160,** 285–299, doi:10.1016/j.jvolgeores.2006.10.002.

Baker, P.E., McReath, I., Harvey, M.R., Roobol, M.J. & Davies, T.G., 1975. *The Geology of the South Shetland Islands: Volcanic Evolution of Deception Island*, Scientific Reports, British Antarctic Survey

Barker, P.F., 1982. The Cenozoic subduction history of the Pacific margin of the Antarctic Peninsula: ridge crest-trench interactions, *J. Geol. Soc. Lond.,* **139,** 787–801.

Benz, H.M., Chouet, B.A., Dawson, P.B., Lahr, J.C., Page, R.A. & Hole, J.A., 1996. Three dimensional P and S wave velocity structure of Redoubt Volcano, Alaska, *J. geophys. Res.,* **101,** 8111–8128.

Ben-Zvi, T., Wilcock, W.S.D., Barclay, A.H., Zandomeneghi, D., Ibáñez, J.M. & Almendros, J., 2009. The P-wave velocity structure of Deception Island, Antarctica, from two-dimensional seismic tomography, *J. Volc. Geotherm. Res.,* **180,** 67–80.

Carmona, E., Almendros, J., Peña, J.A. & Ibáñez, J.M., 2010. Characterization of fracture systems using precise array locations of earthquake multiplets: an example at Deception Island volcano, Antarctica, *J. geophys. Res.,* **115,** B06309, doi:10.1029/2009JB006865.

Dawson, P., Chouet, B., Okubo, P., Villaseñor, A. & Benz, H.M., 1999. Three-dimensional velocity structure of the Kilauea Caldera, Hawaii, *Geophys. Res. Lett.,* **26,** 2805–2808.

De Rosa, R., Mazzuoli, R., Omarini, R.H., Ventura, G. & Viramonte, J.G., 1995. A volcanological model for the historical eruptions at Deception Island (Bransfield Strait, Antarctica), *Terra Antartica,* **2,** 95–101.

Del Pezzo, E., 2008. Seismic wave scattering in volcanoes, in Dmowska, R., Sato, H., Fehler, M. (eds.), Earth heterogeneity and scattering effects on seismic waves, *Adv. Geophys.,* **50,** 353–371.

Del Pezzo, E., La Rocca, M. & Ibáñez, J., 1997. Observations of high-frequency scattered waves using dense arrays at Teide Volcano, *Bull. seism. Soc. Am.,* **87,** 1637–1647.

Frankel, A., Hough, S., Friberg, P. & Busby, R., 1991. Observations of Loma Prieta aftershocks from a dense array in Sunnyvale, California, *Bull. seism. Soc. Am.,* **81,** 1900–1922.

González-Casado, J.M., López-Martínez, J., Giner, J., Duran, J. J. & Gumiel, P., 1999. Análisis de la microfracturación en la Isla Decepción, *Antártida Occidental: Geogaceta,* **26,** 27–30.

Hu, G., Menke, W. & Powell, C., 1994. Polarization tomography for P wave velocity structure in southern California, *J. geophys. Res.,* **99,** 15 245–15 256.

Ibáñez, J.M., Almendros, J., Carmona, E., Martínez-Arévalo, C. & Abril, M., 2003. The recent seismo-volcanic activity at Deception Island volcano, *Deep Sea Res. II,* **50,** 1611–1629.

Ibáñez, J.M., Del Pezzo, E., Almendros, J., La Rocca, M., Alguacil, G., Ortiz, R. & García, A., 2000. Seismovolcanic signals at Deception Island volcano, Antarctica: wave field analysis and source modeling, *J. geophys. Res.,* **135,** 13 905–13 931.

Jousset, P., Neuberg, J. & Sturton, S., 2003. Modeling the time-frequency content of low-frequency volcanic earthquakes, *J. Volc. Geotherm. Res.,* **128,** 201–223.

Koulakov, I., Yudistira, T., Luehr, B.G., Wandono, 2009. P, S velocity and VP/VS ratio beneath the Toba caldera complex (Northern Sumatra) from local earthquake tomography, *Geophys. J. Int.,* **177,** 1121–1139.

Kruger, F., Scherbaum, F., Weber, M. & Schlittenhardt, J., 1996 Analysis of asymmetric multipathing with a generalization of the double-beam method, *Bull. seism. Soc. Am.,* **86,** 737–749.

La Rocca, M., Del Pezzo, E., Simini, M., Scarpa, R. & De Luca, G., 2001. Array analysis of seismograms from explosive sources: evidence for surface waves scattered at the main topographical features, *Bull. seism. Soc. Am.,* **91,** 219–231.

La Rocca, M., Galluzzo, D., Malone, S., McCausland, W., Saccorotti, G. & Del Pezzo, E., 2008. Testing of small-aperture array analysis using well-located earthquakes, and application to the location of deep tremor, *Bull. seism. Soc. Am.,* **98**(2), doi:10.1785/0120060185.

Lees, J.M., 2007. Seismic tomography of magmatic systems, *J. Volc. Geotherm. Res.,* **167,** 37–56.

Luzón, F., Almendros, J. & García Jerez, A., 2010. Shallow structure of Deception Island volcano, Antarctica, from correlations of ambient seismic noise on a dense set of seismic arrays, *Geophys. J. Int.,* submitted.

Martí, J., Vila, J. & Rey, J., 1996. Deception Island (Bransfield Strait, Antartica): an example of volcanic caldera developed by extensional tectonics, *Geol. Soc. Lond. Special Pub.,* **110,** 253–265.

Martínez-Arévalo, C., Bianco, F., Ibáñez, J.M. & Del Pezzo, E., 2003. Shallow seismic attenuation and shear-wave splitting in the short period range of Deception Island volcano (Antarctica), *J. Volc. Geotherm. Res.,* **128,** 89–113.

Martínez-Arévalo, C., Patane, D., Rietbrock, A. & Ibáñez, J.M., 2005. The intrusive process leading to the Mt. Etna 2001 flank eruption: constraints from 3D attenuation tomography, *Geophys. Res. Lett.,* **32,** L21309, doi:10.1029/2005GL 023736.

Métaxian, J.-P., Lesage, P. & Valette, B., 2002. Locating sources of volcanic tremor and emergent events by seismic triangulation: application to Arenal volcano, Costa Rica, *J. geophys. Res.,* **107,** 2243, doi:10.1029/2001JB000559.

Métaxian, J.-P., O'Brien, G.S., Bean, C.J., Valette, B. & Mora, M., 2009. Locating volcano-seismic signals in the presence of rough topography: wave simulations on Arenal volcano, Costa Rica, *Geophys. J. Int.,* **179,** 1547–1557.

Monteiller, V., Got, J.L., Virieux, J. & Okubo, P., 2005. An efficient algorithm for double-difference tomography and location in heterogeneous media, with an application to the Kilauea volcano, *J. geophys. Res.,* **110,** B12306, doi:10.1029/2004JB 003466

Neuberg, J., Pointer, T., 2000. Effects of volcano-topography on seismic broadband waveforms, *Geophys. J. Int.,* **143,** 239–248.

Nisii, V., Saccorotti, G. & Nielsen, S., 2007, Detailed analysis of wave propagation beneath the Campi Flegrei Caldera (Italy), *Bull. seism. Soc. Am.,* **97,** 440–456.

O'Brien, G.S. & Bean, C.J., 2009. Volcano topography, structure and intrinsic attenuation: their relative influences on a simulated 3D visco-elastic wavefield, *J. Volc. Geotherm. Res.,* **183,** 123–137.

Ohminato, T. & Chouet, B., 1997. A free-surface boundary condition for including 3D topography in the finite-difference method, *Bull. seism. Soc. Am.,* **87,** 494–515.

Ortiz, R. *et al.* 1997 *Monitoring of the Volcanic Activity of Deception Island, South Shetland Islands, Antarctica (1986–1995),* pp. 1071–1076, Geological Evolution and Processes, Antarctic Region.

Paredes, C., Pérez-López, R., Giner-Robles, J.L., de la Vega, R., García-García, A. & Gumiel, P., 2006. Distribución espacial y zonificación tectónica de los morfolineamientos en la Isla Decepción (Shetlands del Sur, Antártida), *Geogaceta,* **39,** 75–78.

Park, J., Morgan, J.K., Zelt, C.A., Okubo, P.G., Peters, L. & Benesh, N., 2007. Comparative velocity structure of active Hawaiian volcanoes from 3-D onshore–offshore seismic tomography, *Earth planet. Sci. Lett.,* **259,** 500–516.

Patane, D., Chiarabba, C., Cocina, O., De Gori, P., Moretti, M. & Boschi, E., 2002. Tomographic images and 3D earthquake locations of the seismic swarm preceding the 2001 Mt. Etna eruption: evidence for a dyke intrusion, *Geophys. Res. Lett.,* **29**(10), 1497, doi:10.1029/2001GL014391.

Rey, J., Somoza, L., Martínez-Frías, J., Benito, R. & Martín-Alfageme, S., 1997. Deception Island (Antarctica): a new target for exploration of Fe-Mn mineralization?, *Geol. Soc. Lond. Special Pub.,* **119,** 239–251.

Rey, J., Maestro, A., Somoza, L. & Smellie, J.L., 2002. Submarine morphology and seismic stratigraphy of Port Foster, in *Geology and Geomorphology of Deception Island,* pp. 40–46, eds Smellie, J. L. and López-Martínez, J., British Antarctic Survey GEOMAP Series 6A & 6B.

Ripperger, J., Igel, H. & Wasserman, J., 2003. Seismic wave simulation in the presence of real volcano topography, *J. Volc. Geotherm. Res.,* **128,** 31–44.

Robertson-Maurice, S.D., Wiens, D.A., Shore, P.J., Vera, E. & Dorman, L.M., 2003. Seismicity and tectonics of the South Shetland Islands and Bransfield Strait from a regional broadband seismograph deployment, *J. geophys. Res.,* **108,** 2091, doi:10.1029/2003JB002416.

Saccorotti, G., Almendros, J., Carmona, E., Ibáñez, J.M. & Del Pezzo, E., 2001. Slowness anomalies from two dense seismic arrays at Deception Island volcano, Antarctica, *Bull. seism. Soc. Am.,* **91,** 561–571.

Saccorotti, G., Zuccarello, L., Del Pezzo, E., Ibáñez, J. & Gresta, S., 2004. Quantitative analysis of the tremor wavefield at Etna Volcano, Italy, *J. Volc. Geotherm. Res.,* **136,** 223–245.

Smellie, J.L., 2001. Lithostratigraphy and volcanic evolution of Deception Island, South Shetland Islands, *Antarctic Sci.,* **13,** 188–209.

Tramelli, A., Del Pezzo, E., Bianco, F. & Boschi, E., 2006. 3D scattering image of the Campi Flegrei caldera (Southern Italy): new hints on the position of the old caldera rim, *Phys. Earth planet. Int.,* **155,** 269–280.

Tramelli, A., Del Pezzo, E. & Fehler, M.C., 2009. 3D scattering image of Mt. Vesuvius, *Bull. seism. Soc. Am.,* **99,** 1962–1972.

Vanorio, T., Virieux, J., Capuano, P. & Russo, G., 2005. Three-dimensional seismic tomography from P-wave and S-wave microearthquake travel times and rock physics characterization of the Campi Flegrei Caldera, *J. geophys. Res.,* **110,** B03201, doi:10.1029/2004JB003102.

Vila, J., Martí, J., Ortiz, R., García, A. & Correig, A.M., 1995. Attenuation and source parameters at Deception Island (South Shetland Islands, Antarctica), *Pure Appl. Geophys.,* **144,** 229–250.

Zandomeneghi, D., Barclay, A.H., Almendros, J., Ibáñez, J.M., Wilcock, W.S.D. & Ben-Zvi, T., 2009. Crustal structure of Deception Island volcano from P-wave seismic tomography: tectonic and volcanic implications, *J. geophys. Res.,* **114,** B06310, doi:10.1029/2008JB005599.